A Study of the Aerosol Effect on a Cloud Field with Simultaneous Use of GCM Modeling and Satellite Observation

Kentaroh Suzuki and Teruyuki Nakajima

Center for Climate System Research, University of Tokyo, Tokyo, Japan

Atusi Numaguti

Graduate School of Environmental Earth Sciences, Hokkaido University, Hokkaido, Japan

Toshihiko Takemura

Research Institute for Applied Mechanics, Kyushu University, Fukuoka, Japan

Kazuaki Kawamoto

Research Institute for Humanity and Nature, Kyoto, Japan

Akiko Higurashi

National Institute for Environmental Studies, Tsukuba, Japan

ABSTRACT

The indirect effect of aerosols was simulated by a GCM for nonconvective water clouds and was compared with remote sensing results from the Advanced Very High Resolution Radiometer (AVHRR) satellite-borne sensor for January, April, July, and October of 1990.

The simulated global distribution of cloud droplet radius showed a land–sea contrast and a characteristic feature along the coastal region similar to the AVHRR results, although cloud droplet radii from GCM calculations and AVHRR retrievals were different over tropical marine regions due to a lack of calculation of cloud–aerosol interaction for convective clouds in the present model and also due to a possible error in the satellite retrieval caused by cirrus and broken cloud contamination. The simulated dependence of the cloud properties on the column aerosol particle number was also consistent with the statistics obtained by the AVHRR remote sensing when a parameterization with the aerosol lifetime effect was incorporated in the simulation. The global average of the simulated liquid water path based on the parameterization with the aerosol lifetime effect showed an insignificant dependence on the aerosol particle number as a result of a global balance of the lifetime effect and the wash-out effect. This dependence was contrary to the results of simulations based on the Sundqvist's parameterization without aerosol lifetime effect; that is, the simulated cloud liquid water path showed a decreasing tendency with the aerosol particle number reflecting only the wash-out effect.

1. Introduction

Clouds play an important role in the earth's climate through their effect on the atmospheric radiative processes and the global hydrologic cycle. One of the important properties of clouds significant for the climatic effect is their microphysical structure, because this determines the cloud optical properties and the precipitation production efficiency of the cloud system. It has been known since the 1950s that clouds over land and ocean have systematically different microphysical structures associated with different abundances of aerosols acting as cloud condensation nuclei (CCN; Squires 1958) as well as with the difference in the dynamical condition. Two kinds of indirect effects of atmospheric aerosols acting as CCN have been recognized to modify the cloud microphysical and radiative properties. One is the so-called Twomey effect or the first kind of indirect effect in which an increase in the aerosol particle number concentration causes an increase in the cloud droplet number concentration and a reduction in the droplet radius when the cloud liquid water path is assumed constant. The increase in the cloud particle num-

Corresponding author address: Teruyuki Nakajima, 4-6-1 Komaba, Meguro-ku, Tokyo 153, Japan.
E-mail: teruyuki@ccsr.u-tokyo.ac.jp

ber further induces an increase in the cloud optical thickness and hence the cloud reflectivity (Twomey 1974). The other effect is the so-called lifetime effect or the second kind of indirect effect in which smaller cloud droplets have a longer lifetime before growing into raindrops, leading to an enhancement of the cloud liquid water path. The aerosol-induced reduction in the cloud droplet size is followed by suppression of rainfall production from the cloud and reduced scavenging efficiency of the aerosols (Albrecht 1989).

Large scale signatures of the aerosol effects on cloud optical properties have been observed in the ship trail cloud phenomenon and in the cloud modification by outflow of continental airmasses over coastal regions (Conover 1966; Coakley et al. 1987; Radke et al. 1989; Nakajima and Nakajima 1995). They found that marine cloud reflectivity was enhanced along the ship trajectory and in the continental air flow due to the indirect effect of aerosols resulting from the input of large amounts of CCN into the clean maritime atmosphere. Smoke aerosol particles emitted by biomass burning have also been detected to produce an influence on the cloud optical properties over land as pointed out by Kaufman and Nakajima (1993) for thick clouds and Kaufman and Fraser (1997) for thin clouds. The global features of the land–ocean contrast of cloud optical properties have been revealed by Han et al. (1994) from Advanced Very High Resolution Radiometers (AVHRR) global analysis. More recently, aerosol impacts on the precipitation efficiency of cloud system have also been observed with the Tropical Rainfall Measuring Mission (TRMM). Rosenfeld (1999) reported that the rainfall from tropical convective clouds was inhibited by forest fire smoke over Indonesia and provided the first direct evidence of the effect of aerosols on the precipitation from convective clouds. Similarly, urban and industrial air pollution was also detected to suppress precipitation (Rosenfeld 2000). Masunaga et al. (2002) have pointed out that the vertical stratification of the effective particle radius is significantly modified by the CCN amount.

The above discussion suggests that the human-induced increase in aerosols has produced a significant change in the cloud microphysical structure. The radiative forcing of the anthropogenic indirect effect has been considered to be comparable to but with the opposite sign of the manmade greenhouse gas forcing (Twomey et al. 1984; Charlson et al. 1992). The indirect radiative forcing of anthropogenic aerosols, therefore, needs to be evaluated quantitatively in order to understand and predict global climate change. Some attempts to estimate the aerosol indirect forcing with general circulation models (GCM) have been made in the last several years (Jones et al. 1994; Boucher and Lohmann 1995; Jones and Slingo 1996; Chuang et al. 1997; Lohmann and Feichter 1997; Rotstayn 1999; Lohmann et al. 2000). Satisfactory estimates, however, have not yet been achieved. The radiative forcing of the first kind of indirect effect ranges from 0 to -2 W m^{-2} (Houghton

et al. 1996, 2001), and the second kind of effect has been hardly understood. Uncertainty in the estimate can be attributed to the problems and ambiguities regarding the treatment of aerosols and clouds in the models.

Motivated by this difficulty in understanding the aerosol indirect effect, several observational research projects on this issue have been developed. Han et al. (2002) investigated the correlation between cloud liquid water path and cloud droplet number concentration based on global satellite-retrieved data to find three different behaviors of positive, neutral, and negative correlations between the two parameters. They suggested that the negative correlation is associated with reduction of water vapor supply and cloud liquid water when clouds are decoupled from the boundary layer. Wetzel and Stowe (1999) showed that the cloud droplet size from AVHRR observations is inversely correlated with the aerosol optical thickness over the global ocean, suggesting the critical value of aerosol optical thickness above which the cloud properties did not change. More recently, Nakajima et al. (2001) analyzed AVHRR-retrieved cloud and aerosol microphysical parameters over the global ocean. They found that the cloud particle effective radius and the cloud optical thickness have negative and positive correlations with the column aerosol particle number, respectively, while the liquid water content is approximately constant and independent of the aerosol particle number on a global scale.

There were studies relating the satellite-derived cloud properties with model-calculated aerosol amount. Chameides et al. (2002) examined the correlation between cloud optical depths derived from the International Satellite Cloud Climatology Project (ISCCP) and aerosol burden calculated by a regional climate/chemical transport model over East Asia and found a similarity in the distributions of model-calculated anthropogenic aerosols and ISCCP-derived cloud optical depths. Schwartz et al. (2002) made an effort to detect the enhancement of cloud optical properties caused by aerosols by investigating how the cloud optical depth or albedo depends on liquid water path using model-calculated sulfate loading in mid–North Atlantic region.

These researches have thrown a light on the mechanism of the aerosol and cloud interaction phenomena, but to our knowledge there has been no full comparison between satellite-derived aerosol–cloud interaction global statistics with the corresponding statistics simulated by a global model implemented with the aerosol–cloud interaction process. In the present study, we reinvestigated the results by Nakajima et al. (2001) by comparing those observed aerosol and cloud parameters with simulated values from the Center for Climate System Research (CCSR)/National Institute for Environmental Studies (NIES) atmospheric general circulation model (AGCM) that has been implemented with a new parameterization of cloud–aerosol interaction. The model used in this study is described in section 2, where the conditions and design of the simulation are also

TABLE 1. Particle density and radius of sulfate and carbonaceous aerosols assumed for calculation of aerosol particle number concentration.

Species	Sulfate	Carbonaceous					
Origin		Forest fire (tropical)	Forest fire (other)	Fossil fuel	Fuel wood	Agriculture	Terpene
Density (g cm^{-3})	1.769	1.473	1.468	1.442	1.462	1.468	1.5
Radius (μm)	0.07	0.1					

presented. Satellite-derived data are introduced in section 3. Section 4 presents the simulated results to be compared with the satellite observation. Discussion and conclusions are given in sections 5 and 6, respectively.

2. Model simulation

The GCM used in this study is the CCSR/NIES AGCM (Numaguti 1993; Numaguti et al. 1995). A. Numaguti (1999, personal communication) has updated the model to introduce the aerosol indirect effect into the condensation process representing nonconvective clouds whose temperature is above 273 K, whereas convective clouds including those whose top is lower than 273 K isotherm level or ice clouds are simulated without the aerosol effect. Detailed description of how the aerosol indirect effect was incorporated into the model is presented below.

In the present model, the number concentration of aerosol particles acting as CCN at each model level, $n_a(z)$, is used for calculating the cloud droplet number concentration $n_c(z)$ at the corresponding level. The global distribution of $n_a(z)$ used in this study was calculated by the global three-dimensional aerosol transport model Spectral Radiation-Transport Model for Aerosol Species (SPRINTARS), developed by Takemura et al. (2000, 2002), which simultaneously treats all the major aerosol species, that is, sulfate, carbonaceous, sea salt, and mineral dust aerosols. This aerosol model has been implemented in the CCSR/NIES AGCM. The aerosol number concentration $n_a(z)$ is given as the sum of contributions from sulfate, carbonaceous and sea salt aerosols:

$$n_a(z) = n_{\text{sulfate}}(z) + n_{\text{carbon}}(z) + n_{\text{seasalt}}(z).$$

Mineral dust is excluded from the evaluation of $n_a(z)$ because dust itself is insoluble and regarded as ineffective as CCN, although mixture with other aerosol species such as sulfate or carbonaceous may provide CCN. Simplified treatment of dust aerosol can be a source of error for inferring the cloud particle radius since dust aerosol is abundant in mass concentration in the atmosphere. The number concentration of sulfate aerosol type $n_{\text{sulfate}}(z)$ is evaluated as

$$n_{\text{sulfate}}(z) = \frac{\rho(z)q_{\text{sf}}(z)}{\rho_{\text{sf}}4\pi r_{\text{sf}}^3/3},$$

where $\rho(z)$ denotes the air density, and $q_{\text{sf}}(z)$, ρ_{sf}, and r_{sf} the mass mixing ratio, particle density, and mode

radius of sulfate aerosol, respectively. Here $q_{\text{sf}}(z)$ is evaluated by the aerosol transport model with the values of ρ_{sf} and r_{sf} presented in Table 1. The value of mode radius is that of dry particle, which is same value as those used in the aerosol transport model (Takemura et al. 2002, Table 4). Carbonaceous aerosols are treated as an internal mixture of black carbon (BC) and organic carbon (OC) with the ratio of OC to BC (OC/BC) depending on the origin of the carbonaceous aerosols (Takemura et al. 2000, 2002), and hence the particle density is also somewhat different for each origin as presented in Table 1. Then $n_{\text{carbon}}(z)$ is given by the sum of the contributions from various origins:

$$n_{\text{carbon}}(z) = \sum_i \frac{\rho(z)q_{\text{cb},i}(z)}{\rho_{\text{cb},i}4\pi r_{\text{cb},i}^3/3},$$

where the suffix i identifies the origin of carbonaceous aerosols. The mass mixing ratio $q_{\text{cb},i}(z)$ is evaluated by the aerosol transport model. The values of the particle density $\rho_{\text{cb},i}$ and the mode radius $r_{\text{cb},i}$ are also presented in Table 1. Mode radius is a dry particle radius, which is same value as used in original aerosol transport model (Takemura et al. 2002, Table 4). The number concentration of sea salt aerosol $n_{\text{seasalt}}(z)$ is calculated similarly to the above two species, but as a function of wind velocity over the ocean surface based on the empirical formula of Erickson et al. (1986) with a mode radius estimated by the relationship suggested by Erickson and Duce (1988) (Takemura et al. 2000). The global distribution of $n_a(z)$ is calculated as above for each time step, assuming the background minimum value of 3×10^6 m^{-3}. In the present study, the aerosol distribution was simulated by SPRINTARS, an aerosol transport model implemented to CCSR/NIES AGCM with the standard cloud process parameterization without aerosol indirect effect. In this calculation with SPRINTARS, the wet deposition was driven by cloud and precipitation based on the parameterization of Sundqvist (1978) without aerosol indirect effect and thus not affected by aerosol lifetime effect. This simplification will not produce a significant error in our results, because the CCSR/NIES AGCM standard version has been validated to produce realistic cloud and precipitation fields that are further used in the simulation of aerosol distribution by aerosol transport model (SPRINTARS). In this simulation of aerosol distribution, we further applied a nudging technique with National Centers for Environmental Prediction–National Center for Atmospheric Research

(NCEP–NCAR) reanalysis data to secure a realistic simulation of the meteorological fields such as wind, temperature, and humidity, which are used for simulating the global aerosol distribution properly for our target year of 1990.

In order to calculate the cloud microphysical structure change due to the aerosol indirect effect, the CCSR/NIES AGCM is rerun with the aerosol indirect effect parameterization using the simulated value of $n_a(z)$ as explained above. This second run with indirect effect is performed without nudging technique to investigate how aerosols affect the cloud field in GCM calculation with various atmospheric processes. The cloud droplet number concentration $n_c(z)$ is determined diagnostically by the parameterization with the empirical relationship developed by A. Numaguti (1999, personal communication):

$$n_c(z) = \frac{\varepsilon n_a(z) n_m}{\varepsilon n_a(z) + n_m}, \tag{1}$$

where ε and n_m are prefixed constants. According to this formula, n_c is proportional to n_a when n_a is small compared with n_m, whereas n_c approaches the saturation value n_m with increasing n_a when n_a is comparable or superior to n_m. The range of small n_a corresponds to a clean condition (e.g., over the ocean) and the range of large n_a corresponds to a polluted condition (e.g., over the continent). The values of $\varepsilon = 1$ and $n_m = 4 \times 10^8$ m^{-3} are used to approximate the relationship observed by Martin et al. (1994).

The CCSR/NIES AGCM classifies the total water into liquid water and water vapor assuming a subgrid scale distribution of the total water following the scheme of Le Treut and Li (1991). Based on the liquid water content l determined in this way, the rate of rain production P is calculated as

$$P = -\frac{dl}{dt} = \frac{l}{\tau_p},$$

where τ_p is the relaxation time constant, which represents the time scale of the autoconversion rate l/τ_p. The time constant τ_p has been classically expressed by the bulk parameterization of cloud physics in several ways. One is the classical formula given by Kessler (1969):

$$\tau_p = \tau_p(l) = \frac{\tau_0}{1 - l_c/l},$$

or removing the threshold effect (Sundqvist 1978):

$$\tau_p = \tau_p(l) = \frac{\tau_0}{1 - \exp[-(l/l_c)^2]}. \tag{2}$$

CCSR/NIES AGCM uses this formula (2) in its standard version. According to Sundqvist's formula in Eq. (2), the time constant τ_p depends only on the cloud water content l in such a way that an increase in l shortens the cloud lifetime through decreasing τ_p. Since τ_p does not depend on the cloud particle size in Eq. (2), the

aerosol lifetime effect is not included in this parameterization. The present study performs a simulation with this formula for comparison with other types of parameterization presented below. Values of the constants appearing in Eq. (2) are set as $l_c = 10^{-4}$ kg kg^{-1} and $\tau_0 = 10^4$ s.

There are other types of parameterization that incorporate the effect of cloud droplet number concentration n_c as well as cloud liquid water content l. The classical example for such kind of parameterization is the formula given by Berry (1967), which includes a CCN effect, as

$$\tau_p = \tau_p(l, n_c) = \frac{\beta + \gamma \dfrac{n_c}{\rho l}}{\alpha \rho l}, \tag{3}$$

where ρ is the air density and α, β, and γ are constants. Berry's formula, contrary to that of Kessler or Sundqvist, takes into account the dependency of the conversion rate upon the cloud droplet size as well as the liquid water content and thus includes the lifetime effect of cloud particles due to increasing aerosols. According to this formula, more abundant n_c reduces the droplet mass $\rho l/n_c$, leading to a longer τ_p. We use Eq. (3) with $\alpha = 0.35$, $\beta = 0.12$, and $\gamma = 5.7 \times 10^{-12}$ following Lohmann and Feichter (1997).

Another example of parameterization including the effect of cloud droplet number concentration n_c is the formula suggested by Khairoutdinov and Kogan (2000). They assumed the form,

$$\tau_p = \tau_p(l, n_c) \propto \frac{n_c^\alpha}{l^\beta}, \tag{4}$$

with nondimensional parameters $\alpha = 1.79$ and $\beta = 1.47$ determined from many numerical experiments with a drop spectrum resolving microphysical model. The conversion rate of cloud water into rain water is evaluated with either parameterization, Eqs. (2), (3), or (4) in the present study, to derive the cloud water content $l(z)$ remaining after precipitation. Based on the cloud droplet number concentration $n_c(z)$ and the cloud water content $l(z)$ thus calculated, the cloud droplet radius is calculated as

$$r_c(z) = \left[\frac{3}{4\pi} \frac{\rho l(z)}{\rho_w n_c(z)} \right]^{1/3}, \tag{5}$$

where ρ_w is the liquid water density.

Cloud particle effective radius $r_e(z)$ can be empirically related to $r_c(z)$ as

$$r_e(z) = k^{-1/3} r_c(z),$$

where the parameter k depends on the cloud droplet size distribution function. According to Martin et al. (1994), the value of k is 0.67 ± 0.07 and 0.80 ± 0.07 over the land and ocean, respectively; thus $k^{-1/3}$ is equal to 1.14 (land) and 1.07 (ocean). We choose 1.1 for the value of $k^{-1/3}$ commonly over land and ocean. Using the liquid water content l and the effective radius r_e, the liquid

water path (LWP) and the cloud optical thickness τ_c are calculated by their definitions:

$$\text{LWP} = \int_{\text{bottom}}^{\text{top}} \rho(z)l(z) \, dz \quad \text{and}$$

$$\tau_c = \frac{3}{2} \frac{1}{\rho_w} \int_{\text{bottom}}^{\text{top}} \frac{\rho(z)l(z)}{r_e(z)} \, dz.$$

Based on the model presented above, we performed a numerical simulation of the global cloud–aerosol characteristics with horizontal resolution of about $5.6° \times 5.6°$ (T21) and with 11 levels (σ levels at 0.995, 0.980, 0.950, 0.900, 0.815, 0.679, 0.513, 0.348, 0.203, 0.092, and 0.021). Time integration was performed for 13 months from December 1989 to December 1990 with a time step of 30 min and with the initial condition of temperature and wind fields taken from NCEP–NCAR reanalysis data of 1 December 1989. The simulated results for one year, 1990, are adopted for comparison with satellite observation without those for first month (December 1989) considering the spinup of the model. The year 1990 was selected for the present study to compare the simulation result with the satellite remote sensing results retrieved in the year of 1990 as described in the next section.

3. Satellite data

In the present study, the model-simulated results are compared with the aerosol and cloud microphysical parameters derived from satellite remote sensing. The cloud optical thickness τ_c and particle effective radius r_e in 1990 were derived by the method of Kawamoto et al. (2001) for water clouds whose top temperature is higher than 273 K. Kawamoto et al. (2001), which is an extension of Nakajima and Nakajima (1995) to a global algorithm, developed the algorithm for global determination of the water cloud optical thickness and the particle effective radius from reflected solar spectral radiances in channels 1 and 3 of AVHRR, with an algorithm similar to that of Nakajima and King (1990), after removing thermal radiation emission using channel 3 and 4 radiances. Retrieved r_e and τ_c by Kawamoto et al. (2001) are further used to calculate the cloud liquid water path as

$$\text{LWP} = \frac{2}{3}\rho_w \tau_c r_e. \tag{6}$$

Also used in this study are the aerosol optical thickness τ_a and Ångström exponent α over the global ocean in 1990 also retrieved from AVHRR by the algorithm of Nakajima and Higurashi (1998) and Higurashi and Nakajima (1999), which are the first global satellite analysis of the Ångström parameters utilizing reflected solar spectral radiances in the red and near-infrared channels (channels 1 and 2) of AVHRR. This two-channel algorithm retrieves the peak volume values of the

assumed bimodal size distribution of aerosol particles and then evaluates the aerosol optical properties τ_a at a reference wavelength of 500 nm and Ångström exponent α, the mean wavelength index of the optical thickness spectrum over 369 to 1050 nm. Since the aerosol optical thickness represents the vertical total amount of the aerosol cross section and the Ångström exponent provides information on the aerosol particle size, an estimate of the column particle number N_a is acquired from the approximation proposed by Nakajima et al. (2001).

4. Comparison of GCM simulation with satellite observation

a. Global distribution of cloud particle radius

Figure 1 shows the global map of AVHRR-retrieved (top) and GCM-simulated cloud particle effective radii with Berry's (middle) and Khairoutdinov's (bottom) parameterization for a 4-month (January, April, July, and October) mean condition in 1990. Since the particle radius was mainly determined from the near-infrared radiance of AVHRR reflected by the cloud particle near the cloud top, AVHRR-derived cloud particle effective radii represent those near the cloud top. To match the AVHRR retrieval, the cloud top height is also determined in the GCM simulation by finding the highest level where the liquid water content is larger than a critical value and the temperature is higher than 273 K to avoid ice particles for which the remote sensing algorithm cannot retrieve a precise value of effective particle radius due to nonspherical scattering by irregular ice particles. Shown in the middle and bottom of Fig. 1 is the global distribution of simulated cloud particle effective radii at the cloud top level determined in such a way. The satellite and model values are found to agree with each other regarding the land–ocean contrast. Particle radii over the continent are systematically smaller than those over the ocean as also revealed by previous satellite retrievals such as those of Han et al. (1994) and Kawamoto et al. (2001). The simulated particle radius is significantly reduced even over some coastal ocean regions such as the east coasts of China and North America, the Persian Gulf, the west coast of Africa, and an area off California, as also found by satellite remote sensing. On the other hand, a large effective radius is simulated by GCM over the Northern Hemispheric Atlantic Ocean of mid to high latitudes, where satellite-retrieved values are also large. The zonal belt of large droplet radii over mid to high latitudes in the Southern Hemisphere detected by AVHRR is also found in the GCM calculation. GCM also produced large particle radii over the Amazon basin and equatorial Africa consistently with satellite observation. GCM-simulated results with Berry's and Khairoutdinov's parameterizations, shown in the middle and bottom of Fig. 1, respectively, depict the common characteristics such as
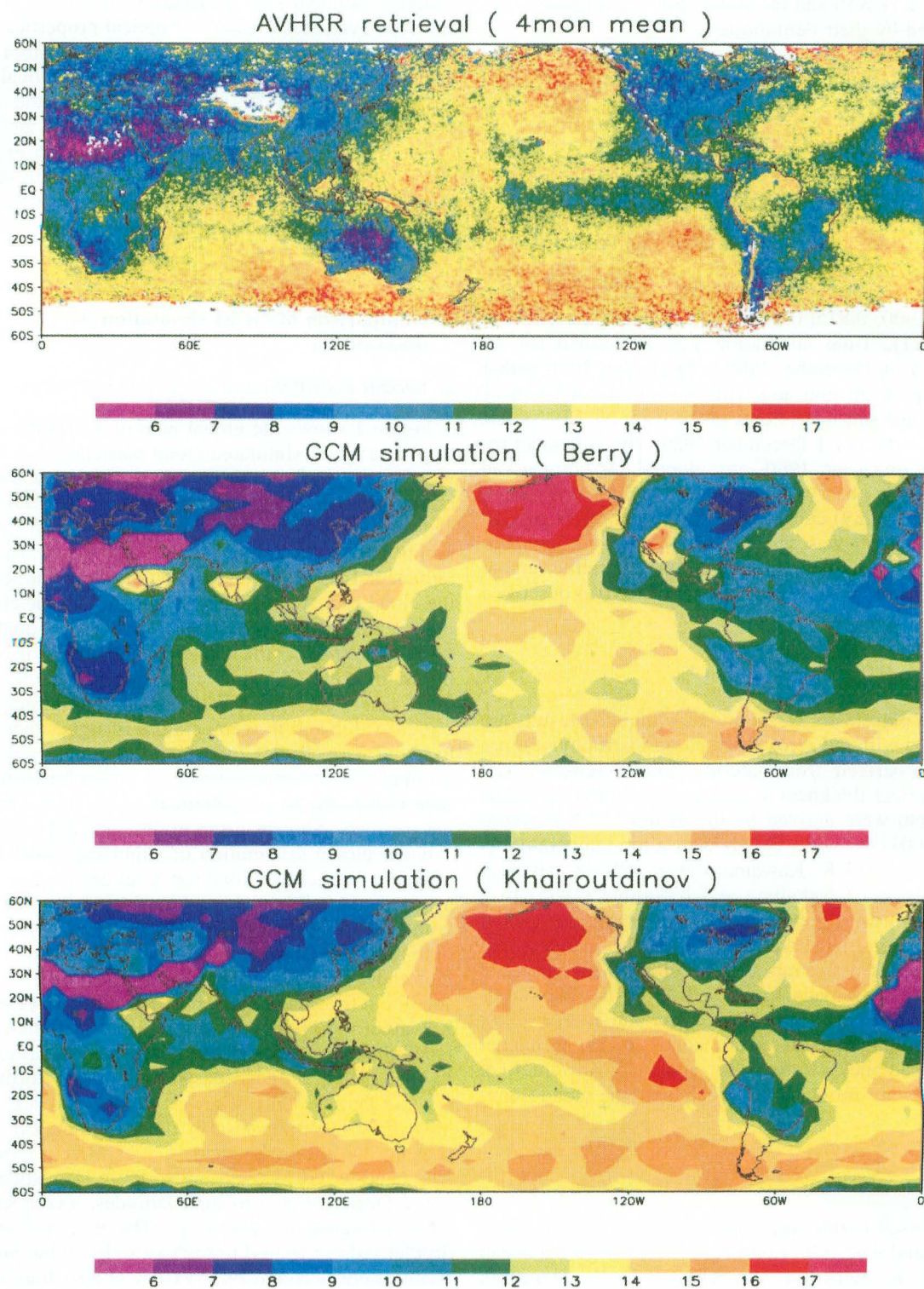
FIG. 1. Four-month (Jan, Apr, Jul, and Oct 1990) mean global distributions of cloud particle effective radii from (top) AVHRR retrieval, (middle) GCM simulation with Berry's parameterization, and (bottom) GCM simulation with Khairoutdinov's parameterization.
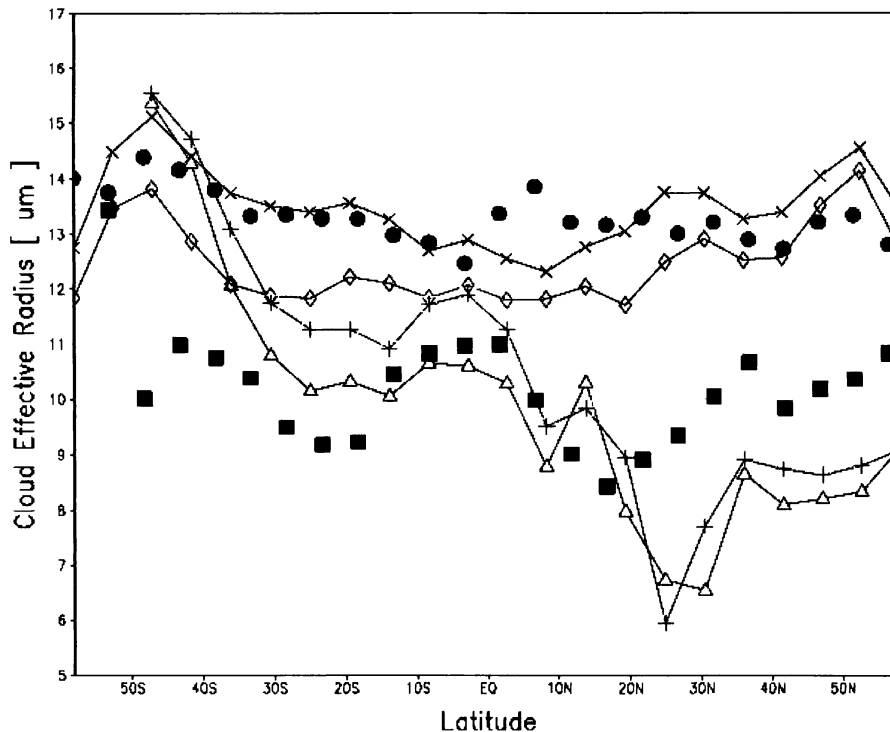
FIG. 2. Latitudinal distributions of zonally averaged cloud particle effective radii over land and ocean from AVHRR retrieval (land: closed square; sea: closed circle), GCM simulation with Berry's parameterization (land: triangle; sea: diamond), and GCM simulation with Khairoutdinov's parameterization (land: +; sea: ×).

land–sea contrast and coastal region feature, although they are somewhat different over ocean areas such as the south Indian Ocean, South Atlantic, and eastern equatorial Pacific where the effective radii calculated from Khairoutdinov's parameterization (bottom) are larger than those from Berry's parameterization (middle). This is because Khairoutdinov's parameterization *given by formula* (4) tends to produce larger remaining cloud water amount over these regions with moderate aerosol abundance as shown in Fig. 3 due to stronger lifetime effect caused by the nonlinear dependence of precipitation time constant τ_p upon N_c, contrary to the linear dependence of Berry's parameterization as given in formula (3). These simulated features from Khairoutdinov's parameterization (bottom) are closer to AVHRR retrieval (top) than those from Berry's parameterization (middle), suggesting that the nonlinear dependency of precipitation time constant on the cloud particle number concentration as given in formula (4) is important for the formation of geographical distribution of cloud particle radii.

Figure 2 shows the latitudinal distribution of cloud effective radii, which is a zonal average from the global map shown in Fig. 1. Over the land, model results tend to underestimate by about 2 μm over Northern Hemisphere (20°–60°N) and overestimate by about 1–3 μm over Southern Hemisphere (20°–60°S). Agreement between model and satellite observation is better over the

ocean where the simulated results from Khairoutdinov's parameterization follow satellite retrieval more closely than those from Berry's parameterization.

In our model, the continental and coastal ocean regions where the droplet radius is simulated to be small correspond to the regions where aerosol particles are abundant as shown in Fig. 3. Simulated land–ocean contrast and the coastal region feature of droplet radius (Fig. 1, middle and bottom) are mainly formed by the distribution of aerosol particles (Fig. 3). Hence, it is concluded that the reduction of cloud particle size is strongly controlled by the aerosol burden in our GCM in a way that is consistent with the satellite observations.

Over the tropical marine region, however, a notable difference was found between the satellite retrievals and the GCM simulation. Although satellite observations generally show large effective radii over the tropical ocean coinciding with the deep-convective precipitation band, such as the intertropical convergence zone (ITCZ) and the South Pacific convergence zone (SPCZ), the GCM does not show such a characteristic. A possible reason for the disparity between satellite and model results is the fact that satellite retrievals tend to overestimate the effective radius over the Tropics for two reasons. At first, the pixels for analysis over the Tropics are not free from contamination by deep convective ice clouds distributed inhomogeneously on a subpixel scale, which are difficult to be removed completely by the
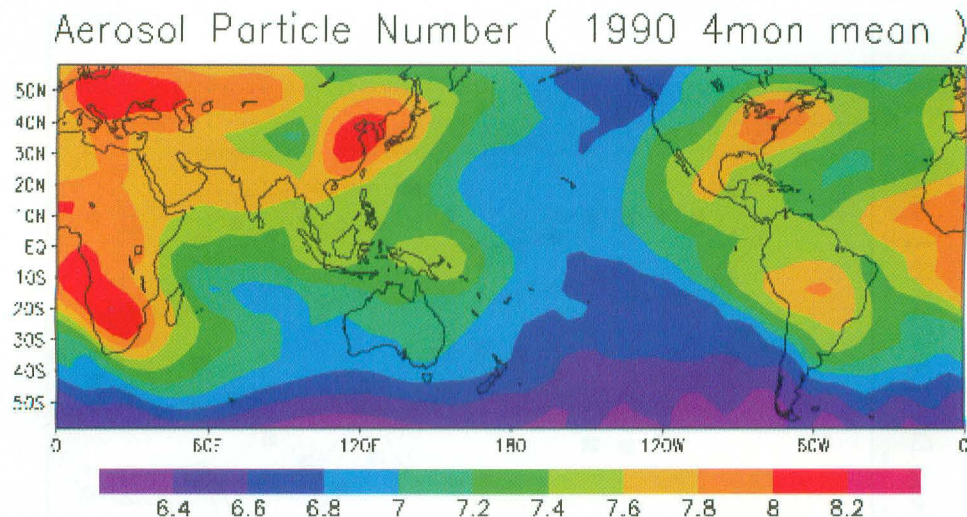
FIG. 3. Four-month (Jan, Apr, Jul, and Oct 1990) mean global distribution of the column aerosol particle number used in the model calculation. The values are expressed on a logarithmic scale of particles per square centimeter.

cloud screening process used in the retrieval algorithm. A second possible reason for the overestimation is contamination by drizzle-sized drops existing in the cloud system, which also lead to larger retrieved values. The disagreement between satellite and GCM results is also partly attributed to insufficient treatment of the indirect effect in our model as it is restricted to nonconvective clouds. It is difficult in our model to represent the character of clouds over the Tropics where deep or shallow convective clouds are predominant.

There is another distinction between satellite and model results over the equatorial Pacific of 100°–170°W, where AVHRR-retrieved effective radii are significantly smaller than those over adjacent marine areas as Kawamoto et al. (2001) pointed out. This region has many partially cloudy pixels excluded from the analysis through the cloud screening process. Kawamoto et al. (2001) suggested that the retrieved result may be affected by statistical biases due to the pixel exclusion over this region. Those disparities between GCM and satellite observation over the tropical region should be discussed in future when indirect effect is incorporated into the convective clouds.

Figure 4 shows frequency distributions of cloud particle effective radii from AVHRR retrieval (top) and GCM simulation with Berry's (middle) and Khairoutdinov's (bottom) parameterization. The relative frequency is drawn over land and ocean separately for both AVHRR and GCM. In Fig. 4, systematic differences of effective radii over land and ocean are illustrated for both satellite observation and model calculations. The simulated distribution of relative frequency with Berry's parameterization over ocean (Fig. 4, middle) has a peak around $r_e = 12$–14 μm, corresponding to the peak found in satellite observation (Fig. 4, top) around $r_e = 13$–14 μm. Mode radii and dispersions of the distribution func-

tions from AVHRR retrieval (top) and GCM simulation with Berry's parameterization (middle) well agree with each other over ocean. In the case of the distribution over land, on the other hand, Berry's case (Fig. 4, middle) shows a narrower and more skewed distribution with a peak at $r_e = 8$ μm, compared with AVHRR retrieval (Fig. 4, top) with a peak around $r_e = 9$–10 μm. This highly skewed simulated distribution seems to bring modeled and satellite-retrieved distributions, shown in Fig. 1, in close agreement along coastal regions of the continents, even with the larger land–ocean difference in the mode radii. In the case of Khairoutdinov's parameterization (Fig. 4, bottom), the frequency distribution over ocean is more skewed toward large particle size than Berry's case (middle) or AVHRR retrieval (top). Simulated frequency distribution with Khairoutdinov's parameterization over land tends to have a secondary maximum over $r_e = 11$–13 μm, which is associated with wider area of large droplet size over the Amazon basin compared with Berry's case as shown in the middle and bottom of Fig. 1. We need more comparisons to conclude these differences are statistically significant.

b. Correlation between cloud properties and aerosol column particle number

In order to quantify the aerosol indirect effect, the correlation between the cloud microphysical properties and the column aerosol particle number is examined in this subsection.

Cloud liquid water path LWP and column cloud particle number N_c are calculated from the satellite-derived cloud data of effective radius r_e and optical thickness τ_c retrieved by the method of Kawamoto et al. (2001). Similarly, the column aerosol particle number N_a is de-
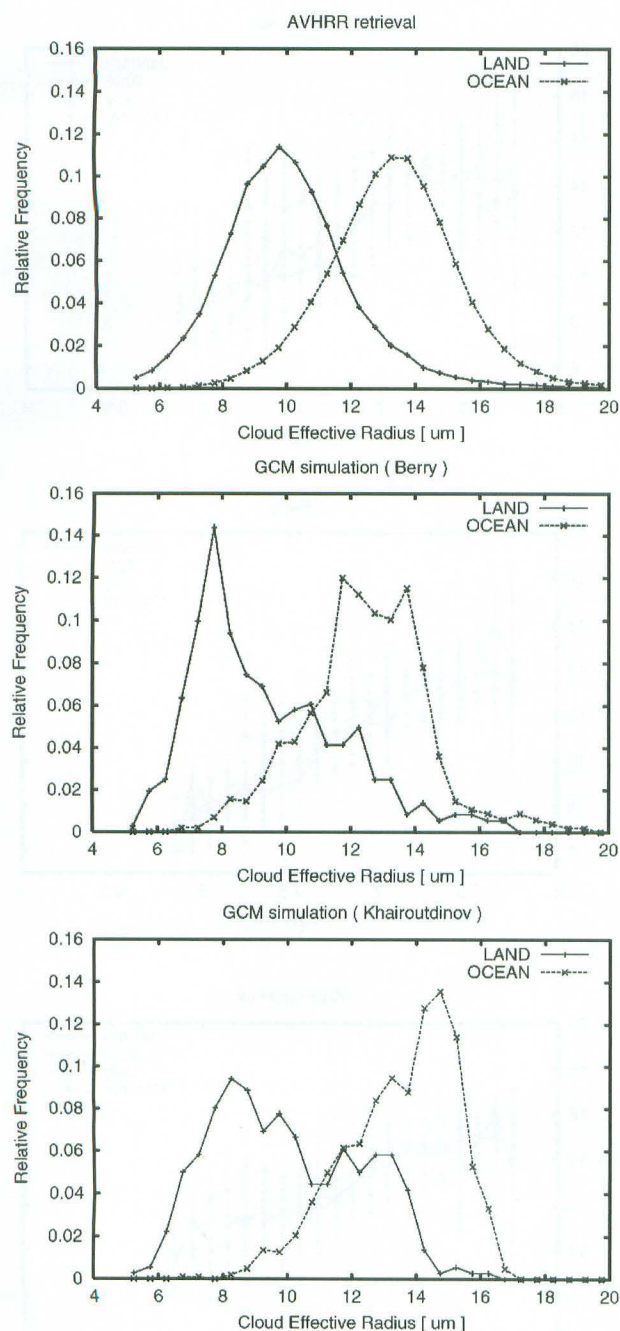
FIG. 4. Frequency distributions of cloud particle effective radii from (top) AVHRR retrieval, (middle) GCM simulation with Berry's parameterization, and (bottom) GCM simulation with Khairoutdinov's parameterization for the same data as used in Fig. 1.

FIG. 5. Scatterplots of (top) cloud effective radius r_e, (middle) optical thickness τ_c, and (bottom) LWP as a function of column aerosol particle number N_a over global ocean for AVHRR retrieval in Jan, Apr, Jul, and Oct 1990.

rived from the aerosol optical thickness τ_a and the Ångström exponent α retrieved by the method of Higurashi and Nakajima (1999). Following Nakajima et al. (2001), Fig. 5 depicts the correlation of the cloud properties r_e (top), τ_c (middle), and LWP (bottom) with the column aerosol particle number N_a, respectively. In this figure, N_a is divided into several bins, and the mean value and
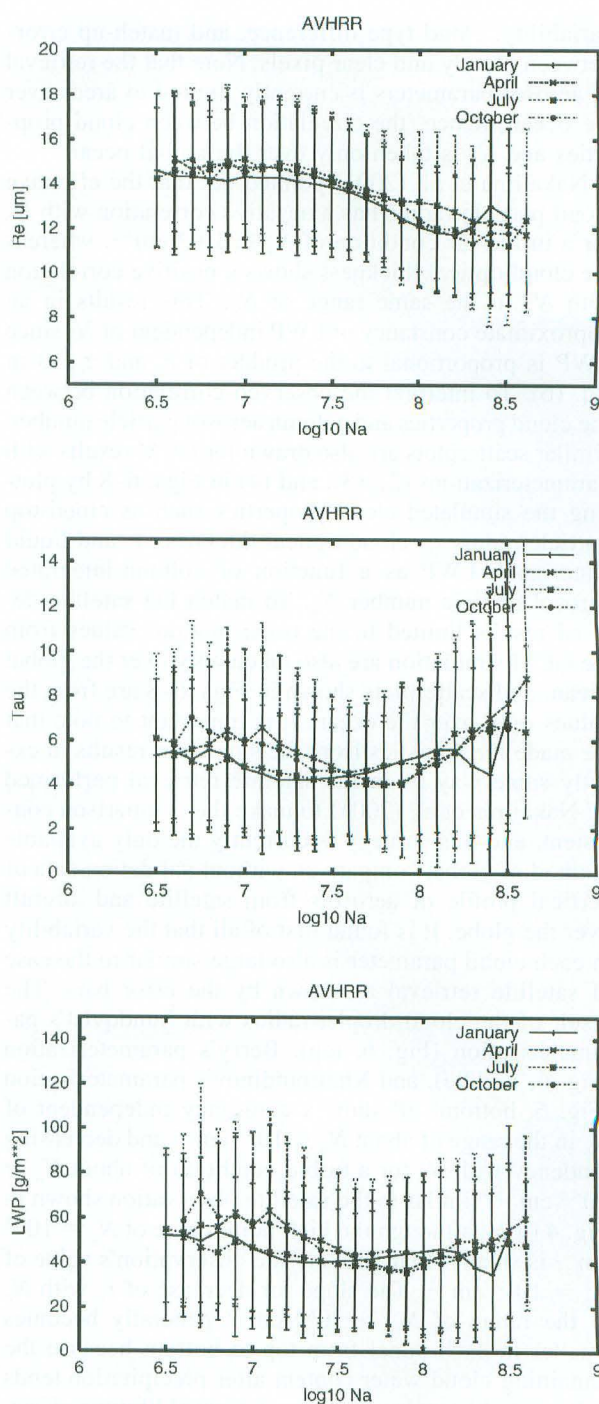
the standard deviation in the properties of each cloud for each bin are plotted as the central point and error bar, respectively. Each cloud parameter shows a large variability for a particular value of N_a, as indicated by the long error bars, for several reasons such as cloud

variability, cloud type difference, and match-up errors between cloudy and clear pixels. Note that the retrieval of aerosol parameters is currently limited to areas over the ocean; hence, the correlation between cloud properties and N_a is taken only over the global ocean.

Nakajima et al. (2001) pointed out that the effective cloud particle radius has a negative correlation with N_a for a turbid air condition of $N_a \geq 10^{7.5}$ cm^{-2}, whereas the cloud optical thickness shows a positive correlation with N_a in the same range of N_a. This results in an approximate constancy of LWP independent of N_a since LWP is proportional to the product of r_e and τ_c, as in Eq. (6). To interpret the observed correlation between the cloud properties and column aerosol particle number, similar scatterplots are also drawn for GCM results with parameterizations (2), (3), and (4) in Figs. 6–8 by plotting the simulated cloud properties such as cloud-top particle radius r_e, cloud optical thickness τ_c and liquid water path LWP as a function of column-integrated aerosol particle number N_a. To match the satellite-derived results limited to the ocean region, values from the GCM simulation are also taken only over the global ocean, and scatterplots shown in Figs. 6–8 are from the values only over the ocean. It is important to note that we made the statistics from the simulated results in exactly same way as in the satellite retrieval performed by Nakajima et al. (2001) to make the comparison consistent, and this strategy is currently the only available method of global comparison without validation data of vertical profile of aerosols from satellite and aircraft over the globe. It is found first of all that the variability in each cloud parameter is also large similar to the case of satellite retrieval as shown by the error bars. The result of the cloud droplet radius with Sundqvist's parameterization (Fig. 6, top), Berry's parameterization (Fig. 6, middle), and Khairoutdinov's parameterization (Fig. 6, bottom) all show a constancy independent of N_a in the range of about $N_a < 10^{6.8}$ cm^{-2} and decreasing tendency with N_a for a turbid condition of about $N_a > 10^{6.8}$ cm^{-2}, similar to the satellite observation shown in Fig. 4 (top), although the kink point value of $N_a = 10^{6.8}$ cm^{-2} is smaller than the satellite observation's value of $N_a = 10^{7.5}$ cm^{-2}. The slope for decrease of r_e with N_a in the range of $N_a > 10^{6.8}$ cm^{-2} generally becomes smaller in each panel from top to bottom because the remaining cloud water content after precipitation tends to become larger due to stronger aerosol lifetime effect, depending on the parameterization used in the simulation (from top to bottom of Fig. 6). Aerosol lifetime effect is not incorporated into Sundqvist's formula (2), and the amplitude of aerosol lifetime effect is larger in Khairoutdinov's formula (4) than in Berry's formula (3) because of the nonlinear dependency of the time constant τ_p upon cloud droplet number concentration N_c in formula (4), contrary to the linearity in formula (3). Simulation with Khairoutdinov's parameterization is closest to the effective cloud particle radius r_e retrieved
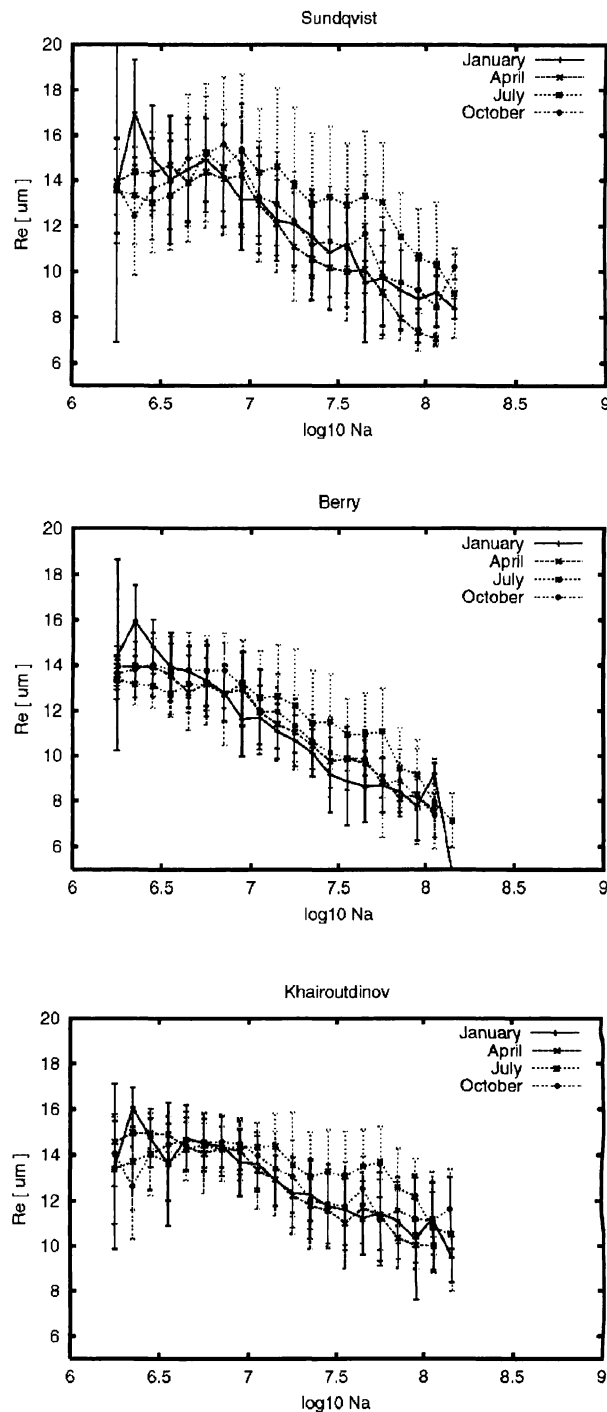

FIG. 6. Scatterplots of cloud effective radius r_e as a function of column aerosol particle number N_a from GCM calculation over global ocean with (top) Sundqvist's parameterization, (middle) Berry's parameterization, and (bottom) Khairoutdinov's parameterization.

from satellite observation especially in terms of slope of r_e decreasing with N_a.

The different dependency of τ_p upon N_c in formulas (2), (3), and (4) is also reflected in the statistics of cloud optical thickness τ_c shown in Fig. 7. A simulated result
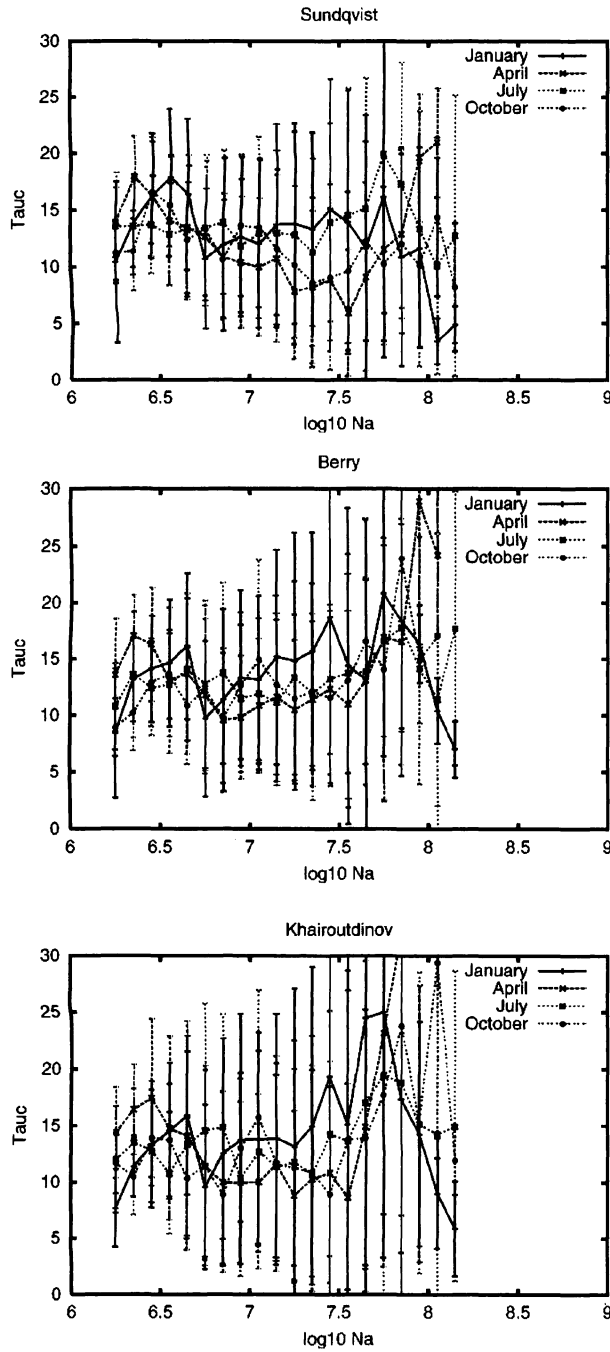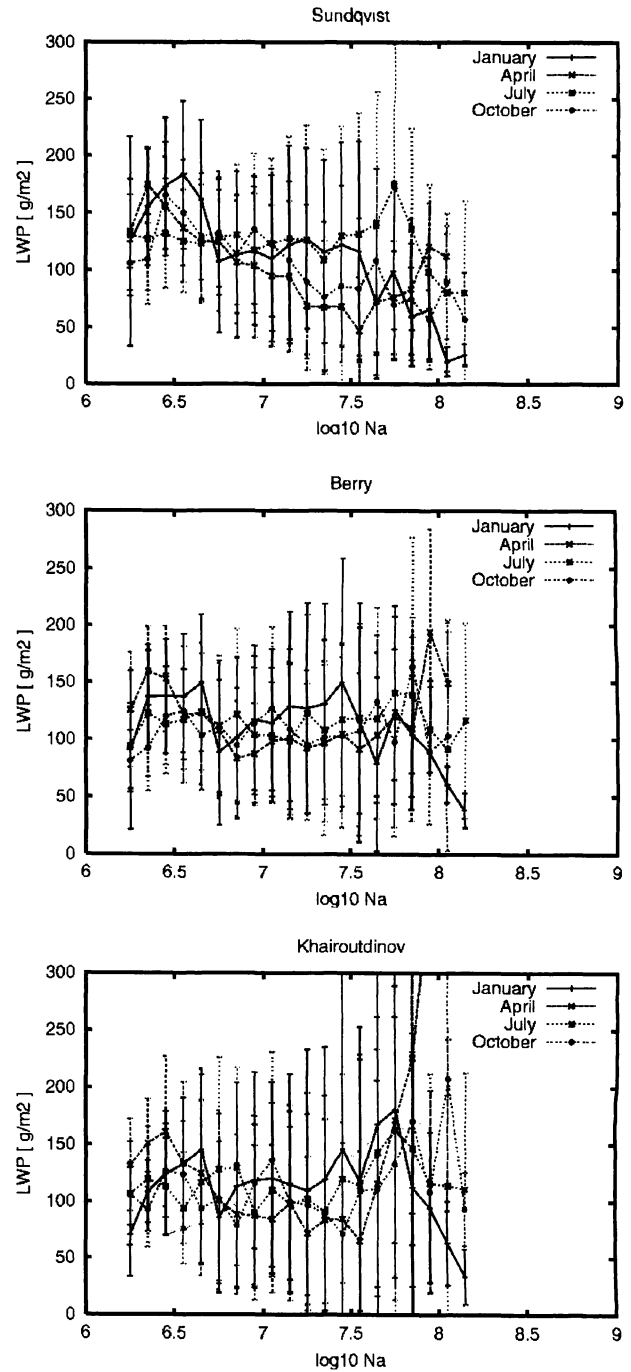
FIG. 7. As in Fig. 6 but for cloud optical thickness τ_c.

FIG. 8. As in Fig. 6 but for liquid water path LWP.

with Sundqvist's parameterization (Fig. 7, top) shows a constancy or a somewhat decrease in τ_c with increasing N_a, which is qualitatively different from the feature found in the simulation with Berry's (Fig. 7, middle) or Khairoutdinov's (Fig. 7, bottom) parameterization. The latter two cases show a common characteristic that τ_c generally tends to be independent of N_a for a clean condition of about $N_a < 10^{7.2}$ cm^{-2} and increase with N_a in the range of about $N_a > 10^{7.2}$ cm^{-2}, which is

consistent with satellite observations (Fig. 5, middle) showing an approximate constancy of τ_c in the range of about $N_a < 10^{7.8}$ cm^{-2} and increasing tendency of τ_c in the range of about $N_a > 10^{7.8}$ cm^{-2} as pointed out by Nakajima et al. (2001). The correlation pattern in the case of Berry's parameterization (Fig. 7, middle) and Khairoutdinov's parameterization (Fig. 7, bottom) are somewhat different from each other for the turbid con-

dition of $N_a > 10^{7.2}$ cm^{-2}. The amplitude of increasing tendency for each month is larger in Khairoutdinov's case (Fig. 7, bottom) than in Berry's case (Fig. 7, middle), reflecting the nonlinearity in Khairoutdinov's formula (4) in contrast to linearity in Berry's formula (3).

A difference between these three parameterizations is also found in the liquid water path LWP. Figure 8 shows scatterplots between LWP and N_a derived from the simulation with parameterizations of Sundqvist (top), Berry (middle), and Khairoutdinov (bottom). According to satellite-derived scatterplots of LWP with N_a shown in bottom of Fig. 5, LWP tends to be approximately constant and independent of N_a as pointed out by Nakajima et al. (2001), although they show some variability such as, for example, decreasing with N_a over the range of $N_a < 10^{7.5}$ cm^{-2}, if the curve is looked at in detail. Such kind of detailed variability is also found in the model-simulated scatterplots with various parameterizations shown in Fig. 8. The top of Fig. 8 shows that LWP derived from Sundqvist's parameterization globally tends to decrease with N_a, whereas the result Berry's case (Fig. 8, middle) shows that LWP tends to be approximately constant and independent of N_a, similar to the case of satellite retrieval (Fig. 5, bottom). This difference in the LWP behavior between Sundqvist's and Berry's parameterization is the result of the different treatment of the conversion rate of cloud water into rain water. According to Sundqvist's parameterization given by formula (2), the conversion rate depends only on the cloud water content without dependence on the cloud droplet number concentration or cloud droplet size; that is, it does not include the aerosol lifetime effect. Greater cloud water amount causes more in-cloud scavenging and wash out; therefore, a lower number of aerosol particles will remain after these processes, leading to the decreasing tendency of LWP with N_a. Berry's parameterization given by formula (3), which includes the aerosol lifetime effect, on the contrary, assumes that the autoconversion rate depends not only on the cloud water content l but also on the cloud droplet number concentration n_c. The autoconversion rate decreases with increasing n_c through the reduction of cloud droplet mass $\rho l / n_c$. Since an increase in aerosol number concentration n_a leads to an increase in n_c in Numaguti's formulation in Eq. (1), greater n_a causes a reduction of the autoconversion rate and thus leads to more cloud water amount remaining after less precipitation. Therefore, the aerosol lifetime effect included in Berry's parameterization produces a positive dependency of LWP on N_a. In-cloud scavenging and wash-out processes, which cause a negative correlation, are also significant in the case of Berry's parameterization, and thus the resultant correlations between LWP and N_a is a mixture of positive and negative correlations produced by the aerosol lifetime effect and the wash-out effect, respectively. The global constancy of LWP independent of N_a shown in the middle of Fig. 8 illustrates that those two opposing effects are nearly balanced on a global scale in the pres-

TABLE 2. The values of regression coefficients A and B determined by the least squares method to fit the scatterplot of LWP and N_a for AVHRR retrieval and GCM simulations with various parameterizations (see text for detail). Uncertainty ranges are also shown at the 95% significance level.

	A (g m^{-2})	B (g m^{-2})
AVHRR retrieval	58.96 ± 1.45	−2.05 ± 0.19
GCM (Sundqvist)	395.71 ± 15.31	−39.84 ± 2.18
GCM (Berry)	263.14 ± 16.21	−22.82 ± 2.31
GCM (Khairoutdinov)	145.19 ± 20.07	−5.05 ± 2.86

ent simulation with Berry's parameterization. The satellite-derived result (Fig. 5, bottom) also shows a similar tendency of constant LWP, suggesting that Berry's parameterization is more suitable than Sundqvist's parameterization to simulate the slope of observed LWP as a function of N_a, although the absolute value of LWP over the range of $N_a > 10^{7.5}$ cm^{-2} from Sundqvist's parameterization tends to be closer to the satellite value than those from Berry's parameterization, which tends to overestimate LWP compared the with satellite observation. The simulated result with Khairoutdinov's parameterization (Fig. 8, bottom) also shows that LWP tends to be constant with N_a due to the global balance of the wash-out effect and the aerosol lifetime effect, similar to the Berry's case, but the variability of LWP with N_a is somewhat larger than Berry's case (Fig. 8, middle), and LWP over the range of about $N_a > 10^{7.5}$ cm^{-2} (Fig. 8, bottom) is larger than LWP derived from Berry's parameterization over the same range of N_a (Fig. 8, middle), which is the result of nonlinear dependency of precipitation time constant τ_p upon the cloud droplet number concentration N_c. The correlation pattern between LWP and N_a is fitted by a linear regression line as

$$\text{LWP} = A + B \log_{10}(N_a),$$

with coefficients A and B summarized in Table 2. The ranges of uncertainty in these coefficients are also shown at the significance level of 95% in Table 2. These uncertainties in the regression coefficients A and B are relatively small compared with the difference of the mean values among the various parameterizations, suggesting that the simulated correlation patterns from various parameterizations have characteristic tendencies systematically different from each other. The result of this statistical analysis summarized in Table 2 suggests that Khairoutdinov's parameterization is closest to the AVHRR retrieval in terms of values of A and B determined for the best fit, implying that the nonlinear representation of aerosol lifetime effect as given in formula (4) is significant for reproducing the satellite-derived global correlation between LWP and N_a.

c. Indirect radiative forcing

Using the parameterizations mentioned above, we estimate anthropogenic indirect radiative forcing with the

use of radiation code based on a two-stream discrete ordinate method (DOM)/adding and a correlated-k distribution method (Nakajima et al. 2000), which is implemented in the CCSR/NIES AGCM.

We define the total indirect radiative forcing $\Delta F_{\text{indirect}}$ as the difference of cloud radiative forcing (CRF) between conditions of present and preindustrial aerosol number concentrations:

$$\Delta F_{\text{indirect}} = \text{CRF}_{\text{present}} - \text{CRF}_{\text{preindustrial}},$$

where CRF is defined as the difference of radiative fluxes between whole sky condition and clear sky condition:

$$\text{CRF} = F_{\text{whole sky}} - F_{\text{clear sky}}.$$

The total indirect radiative forcing $\Delta F_{\text{indirect}}$ is induced by the change in cloud particle radius, cloud water content, and cloud fraction due to the increase in anthropogenic aerosols since the preindustrial era. The preindustrial aerosol distribution is evaluated by SPRINTARS with surface aerosol emissions of natural origin to determine the preindustrial cloud field by CCSR/NIES AGCM with indirect effect. Assumed aerosols of natural origin are dust aerosol, sea salt particle, sulfate aerosol of natural origin (emitted from dimethyl sulfide and volcanic eruption), carbonaceous aerosols originating from forest fire and fuel wood consumption with amount less than the present, and from combustion of agricultural wastes and gas to particle conversion of terpene emitted from plants. Annual global mean total forcing defined as above is calculated to be −1.00 W m^{-2} caused by perturbation of aerosol total number concentration from $n_a = 10^{7.0}$ m^{-3} in the preindustrial condition to $n_a = 10^{7.3}$ m^{-3} in the current condition as the annual global average. The radiative forcing due to only the change of cloud particle radius (i.e., Twomey effect) between the present and preindustrial aerosol condition was also estimated by giving the same aerosol distribution to the cloud scheme, in which the autoconversion rate depends on the cloud droplet number concentration, for both preindustrial and present simulation. In this calculation, different aerosol distributions between the preindustrial and present condition are assumed only in the radiation calculation in order to realize the condition that only cloud particle effective radii are different between the preindustrial and present simulation. The annual global mean forcing thus estimated is −0.54 W m^{-2}, which is about half of the total radiative forcing. The estimated value of total forcing in this study, −1.00 W m^{-2}, is somewhat smaller than those of several previous works. Lohmann and Feichter (1997) estimated the total indirect forcing to range from −1.4 to −4.8 W m^{-2} depending on different cloud schemes. Rotstayn (1999) evaluated the total forcing as −2.1 W m^{-2}. According to Lohmann et al. (2000), the total indirect forcing was estimated as −1.1 and −1.5 W m^{-2} for an internal and external mixture of aerosol, respectively. The calculated forcing due to only the Twomey effect in the present study, −0.54 W m^{-2}, is also smaller than

the averaged value suggested by previous studies, but is within their range and also in the uncertainty range proposed by Houghton et al. (2001). According to several previous studies, such as Jones et al. (1994), Boucher and Lohmann (1995), Jones and Slingo (1996), and Chuang et al. (1997), estimated values of forcing due to the Twomey effect ranges from −0.5 to −1.6 W m^{-2} depending on the relationship between aerosol and cloud droplet number concentration and the parameterization of cloud physics. The ratio of the forcing due to only the Twomey effect to the total forcing acquired by the present study is, however, consistent with those of Rotstayn (1999), which evaluated contribution from the Twomey effect and lifetime effect as −1.2 and −1.0 W m^{-2}, respectively. It is possible that our simulation without full coupling of aerosol, cloud, and precipitation causes a large error in estimation of the radiative forcing, so the fully coupled simulation is necessary for more realistic estimate of indirect radiative forcing.

5. Discussion

The study in the previous section found that the global constancy of LWP in the satellite result can be reproduced by the GCM simulation with Berry's and Khairoutdinov's parameterizations. In this regard, it is interesting to recognize characteristic undulations appearing in the LWP dependence on the aerosol particle number in Fig. 5 (bottom). It appears that LWP has a bimodal feature with two peaks around $N_a \approx 10^{6.6}-10^{7.1}$ cm^{-2} and $N_a \approx 10^{8}-10^{8.5}$ cm^{-2}. More specifically, the curve for January has two peaks around $N_a \approx 10^{6.7}-10^{6.9}$ cm^{-2} and $N_a \approx 10^{8}-10^{8.2}$ cm^{-2}; the curves for April has peaks around $N_a \approx 10^{6.9}-10^{7.1}$ cm^{-2} and $N_a \approx 10^{8.4}-10^{8.6}$ cm^{-2}; the curve for July has peaks around $N_a \approx 10^{6.8}-10^{7}$ cm^{-2} and $N_a \approx 10^{8.2}-10^{8.3}$ cm^{-2}; the curves for October has peaks around $N_a \approx 10^{6.6}-10^{6.8}$ cm^{-2} and $N_a \approx 10^{8.3}-10^{8.5}$ cm^{-2}. It is also interesting to find similar characteristics in the simulated LWP, as shown in the middle of Fig. 8, for example, with two peaks around $N_a \approx 10^{6.4}-10^{6.8}$ cm^{-2} and $N_a \approx 10^{7.5}-10^{8}$ cm^{-2}. It is found that the curve for January has two peaks around $N_a \approx 10^{6.3}-10^{6.6}$ cm^{-2} and $N_a \approx 10^{7.3}-10^{7.4}$ cm^{-2}; the curve for April has peaks around $N_a \approx 10^{6.3}-10^{6.4}$ cm^{-2} and $N_a \approx 10^{7.9}$ cm^{-2}; the curve for July has peaks around $N_a \approx 10^{6.4}-10^{6.6}$ cm^{-2} and $N_a \approx 10^{7.7}-10^{7.8}$ cm^{-2}; the curve for October has peaks around $N_a \approx 10^{6.4}-10^{6.6}$ cm^{-2} and $N_a \approx 10^{7.6}-10^{7.8}$ cm^{-2}. The satellite retrieval produces the first peak for $N_a \approx 10^{6.6}-10^{7.1}$ cm^{-2} located around remote oceanic areas and the second peak for $N_a \approx 10^{8}-10^{8.5}$ cm^{-2} around coastal ocean regions exposed to the aerosol injection from continental regions. On the other hand, the first peak for $N_a \approx 10^{6.4}-10^{6.8}$ cm^{-2} in the GCM simulation found in Fig. 8 (middle) is located around high latitudes and therefore corresponds to the signal of polar clouds as shown in Fig. 3, contrary to the satellite remote sensing results. On the other hand, the second peak for $N_a \approx$

$10^{7.5}$–10^8 cm^{-2} is located around the coastal marine areas, as shown in Fig. 3, where a large amount of aerosols is transported from adjacent continents as is consistent with the satellite results. This investigation suggests that the present GCM simulation was able to simulate the continental peak but did not reproduce the maritime peak found in the satellite result. We cannot identify the reason for this disparity, other than pointing out that there are no concrete reasons why the present GCM reproduces the delicate balance in the CCN and drizzle *particle budget* to simulate the peaked feature in the LWP–N_a plot with the simplified model parameterizations and the large grid size. In particular, the present simulation was based on the simplification without the fully coupled calculation of the aerosol concentration used for calculating the cloud microphysical change. We might need a fully coupled GCM including feedback between aerosols and clouds in order to reproduce the detailed structure of the LWP as a function of the column aerosol particle number. Baker and Charlson (1990) suggested a bistability of the CCN number concentration corresponding to maritime and continental cloud regimes for which different CCN sink processes are responsible for producing the peaks in the cloud formation stability. The maritime mode is accompanied by large-sized drizzle particles or raindrops along with the washout process as a sink to maintain a low CCN number concentration, as also discussed by Albrecht (1989), whereas the continental mode is characterized by a high CCN number concentration without precipitation due to the aerosol lifetime effect. We should conduct more studies to investigate how theories can interpret the peaked feature in the LWP–N_a plot.

The imperfection of the present model is also depicted by the large difference in the absolute values of LWP and N_a between model and satellite results. Also, the sensitivity study for evaluating the range of uncertainty needs to be performed in the near future based on the simulation with various types of relationships between N_a and N_c (e.g., Menon et al. 2002) including those that incorporate the effect of upward velocity (e.g., Ghan et al. 1993) other than that of Martin et al. (1994) used in the present study. Although dust aerosol was excluded from the evaluation of CCN number concentration in the present study because of its inefficiency of acting as CCN, they are considered to become CCN when they are internally mixed with other species such as organic carbon and sulfate under some condition. The increase in knowledge of such kind of phenomena will enable us to treat dust particles properly in the simulation of cloud–aerosol interaction in the future.

6. Conclusions

In this paper, we studied the aerosol indirect effect simulated by the CCSR/NIES AGCM to compare with AVHRR retrievals for water clouds. The simulated distribution was found to be consistent with the satellite retrieval over the ocean region except for the Tropics. The cloud particle effective radius was simulated to be systematically smaller over land and coastal ocean areas stemming from the aerosol injection than that over the remote ocean, as also revealed by the satellite retrieval. The simulated distribution of the cloud particle radius reflected the distribution of aerosol particle number. Tropical regions, where convective clouds prevail, however, were simulated to be different from the satellite retrieval, partly because our calculation was only for nonconvective clouds and also because the satellite retrieval tends to overestimate the particle radius over the Tropics due to contamination by ice and drizzle particles. Simulation and satellite retrieval were also different over the equatorial central Pacific where satellite observations are affected by statistical biases due to problems caused by partial cloudiness. Small-scale convective clouds need to be taken into consideration to represent the cloud droplet size over these regions.

The apparent correlation between the cloud microphysical and optical properties and the column aerosol particle number was also compared between satellite retrievals and model simulations. Simulations with parameterization including the aerosol lifetime effect showed features closer to the satellite retrieval data than that with Sundqvist's parameterization, which does not include the lifetime effect by aerosols. The cloud optical thickness calculated based on Berry's and Khairoutdinov's formulas was positively correlated with N_a for a turbid air condition similar to the satellite retrieval, whereas those with Sundqvist's formula tended to be constant or would decrease with N_a. As a result, the cloud liquid water path tends to be globally constant for the case with Berry's and Khairoutdinov's parameterizations due to the global balance of the wash-out effect and the aerosol lifetime effect, contrary to the negative correlation in the case with Kessler's parameterization because only the wash-out process is included. It was suggested, therefore, that the satellite-derived global constancy of LWP implies a significant role of the aerosol lifetime effect in the formation of the global cloud field. We should emphasize in this regard that this global constancy of the LWP is not the same condition as in a fixed LWP assumption employed by the microphysics studies for an isolated airmass such as in Twomey (1974) because our finding is a manifestation of the large-scale nonlinear balance between the aerosol lifetime effect and the wash-out effect. The indirect radiative forcing estimated in this study, -1 W m^{-2}, is smaller than those acquired from previous studies. One possible reason is our offline calculation of the aerosol distribution without full coupling with cloud and precipitation processes. Fully coupled simulation is necessary for more plausible evaluation of radiative forcing.

ration (JST). We dedicate this paper to the memory of our coauthor, Prof. Atusi Numaguti, who passed away in June 2001.

REFERENCES

Albrecht, B. A., 1989: Aerosols, cloud microphysics, and fractional cloudiness. *Science*, **245**, 1227–1230.

Baker, M. B., and R. J. Charlson, 1990: Bistability of CCN concentrations and thermodynamics in the cloud-topped boundary layer. *Nature*, **345**, 142–145.

Berry, E. X., 1967: Cloud droplet growth by collection. *J. Atmos. Sci.*, **24**, 688–701.

Boucher, O., and U. Lohmann, 1995: The sufate–CCN–cloud albedo effect: A sensitivity study with two general circulation models. *Tellus*, **47B**, 281–300.

Chameides, W. L., C. Luo, R. Saylor, D. Streets, Y. Huang, M. Bergin, and F. Giorgi, 2002: Correlation between model-calculated anthropogenic aerosols and satellite-derived cloud optical depths: Indication of indirect effect? *J. Geophys. Res.*, **107**, 4085, doi: 10.1029/2000JD000208.

Charlson, R. J., S. E. Schwartz, J. M. Hales, R. D. Cess, J. J. A. Coakley, J. E. Hansen, and D. J. Hofmann, 1992: Climate forcing by anthropogenic aerosols. *Science*, **255**, 423–430.

Chuang, C. C., J. E. Penner, K. E. Taylor, and A. S. Grossman, 1997: An assessment of the radiative effects of anthropogenic sulfate. *J. Geophys. Res.*, **102**, 3761–3778.

Coakley, J., A. James, R. L. Bernstein, and P. A. Durkee, 1987: Effect of ship-stack effluents on cloud reflectivity. *Science*, **237**, 1020–1022.

Conover, J. H., 1966: Anomalous cloud lines. *J. Atmos. Sci.*, **23**, 778–785.

Erickson, D. J., and R. A. Duce, 1988: On the global flux of atmospheric sea salt. *J. Geophys. Res.*, **93**, 14 079–14 088.

——, T. Merrill, and R. A. Duce, 1986: Seasonal estimates of global atmospheric sea-salt distribution. *J. Geophys. Res.*, **91**, 1067–1072.

Ghan, S. J., C. C. Chuang, and J. E. Penner, 1993: A parameterization of cloud droplet nucleation. Part I: Single aerosol type. *Atmos. Res.*, **30**, 197–222.

Han, Q., W. B. Rossow, and A. A. Lacis, 1994: Near-global survey of effective droplet radii in liquid water clouds using ISCCP data. *J. Climate*, **7**, 465–497.

——, ——, J. Zeng, and R. Welch, 2002: Three different behaviors of liquid water path of water clouds in aerosol–cloud interactions. *J. Atmos. Sci.*, **59**, 726–735.

Higurashi, A., and T. Nakajima, 1999: Development of a two-channel aerosol retrieval algorithm on a global scale using NOAA AVHRR. *J. Atmos. Sci.*, **56**, 924–941.

Houghton, J. T., L. G. Meira Filho, B. A. Callander, N. Harris, A. Kattenberg, and K. Maskell, Eds., 1996: *Climate Change 1995: The Science of Climate Change.* Cambridge University Press, 572 pp.

——, Y. Ding, D. J. Griggs, M. Noguer, P. J. van der Linden, X. Dai, K. Maskell, and C. A. Johnson, Eds., 2001: *Climate Change 2000: The Science of Climate Change.* Cambridge University Press, 881 pp.

Jones, A., and A. Slingo, 1996: Predicting cloud-droplet effective radius and indirect sulphate aerosol forcing using a general circulation model. *Quart. J. Roy. Meteor. Soc.*, **122**, 1573–1595.

——, D. L. Roberts, and A. Slingo, 1994: A climate model study of indirect radiative forcing by anthropogenic sulphate aerosols. *Nature*, **370**, 450–453.

Kaufman, Y. J., and T. Nakajima, 1993: Effect of amazon smoke on cloud microphysics and albedo—Analysis from satellite imagery. *J. Appl. Meteor.*, **32**, 729–744.

——, and R. S. Fraser, 1997: The effect of smoke particles on clouds and climate forcing. *Science*, **277**, 1636–1639.

Kawamoto, K., T. Nakajima, and T. Y. Nakajima, 2001: A global

determination of cloud microphysics with AVHRR remote sensing. *J. Climate*, **14**, 2054–2068.

Kessler, E., 1969: *On the Distribution and Continuity of Water Substance in Atmospheric Circulations. Meteor. Monogr.*, No. 32, Amer. Meteor. Soc., 84 pp.

Khairoutdinov, M., and Y. Kogan, 2000: A new cloud physics parameterization in a large-eddy simulation model of marine stratocumulus. *Mon. Wea. Rev.*, **128**, 229–243.

Le Treut, H., and Z.-X. Li, 1991: Sensitivity of an atmospheric general circulation model to prescribed SST changes: Feedback effects associated with the simulation of cloud optical properties. *Climate Dyn.*, **5**, 175–187.

Lohmann, U., and J. Feichter, 1997: Impact of sulfate aerosols on albedo and lifetime of clouds: A sensitivity study with the ECHAM4 GCM. *J. Geophys. Res.*, **102**, 13 685–13 700.

——, ——, J. Penner, and R. Leaitch, 2000: Indirect effect of sulfate and carbonaceous aerosols: A mechanistic treatment. *J. Geophys. Res.*, **105**, 12 193–12 206.

Martin, G. M., D. W. Johnson, and A. Spice, 1994: The measurement and parameterization of effective radius of droplet in warm stratocumulus clouds. *J. Atmos. Sci.*, **51**, 1823–1842.

Masunaga, H., T. Y. Nakajima, T. Nakajima, M. Kachi, and K. Suzuki, 2002: Physical properties of maritime low clouds as retrieved by combined use of TRMM Microwave Imager and Visible/Infrared Scanner. II. Climatology of warm clouds and rain. *J. Geophys. Res.*, **107**, 4367, doi:10.1029/2001JD001269.

Menon, S., A. D. del Genio, D. Koch, and G. Tselioudis, 2002: GCM simulations of the aerosol indirect effect: Sensitivity to cloud parameterization and aerosol burden. *J. Atmos. Sci.*, **59**, 692–713.

Nakajima, T., and M. D. King, 1990: Determination of the optical thickness and effective particle radius of clouds from reflected solar radiation measurements. Part I: Theory. *J. Atmos. Sci.*, **47**, 1878–1893.

——, and A. Higurashi, 1998: A use of two-channel radiances for an aerosol characterization from space. *Geophys. Res. Lett.*, **25**, 3815–3818.

——, M. Tsukamoto, Y. Tsushima, A. Numaguti, and T. Kimura, 2000: Modeling of the radiative processes in an atmospheric general circulation model. *Appl. Opt.*, **39**, 4869–4878.

——, A. Higurashi, K. Kawamoto, and J. E. Penner, 2001: A possible correlation between satellite-derived cloud and aerosol microphysical parameters. *Geophys. Res. Lett.*, **28**, 1171–1174.

Nakajima, T. Y., and T. Nakajima, 1995: Wide-area determination of cloud microphysical properties from NOAA AVHRR measurements for FIRE and ASTEX regions. *J. Atmos. Sci.*, **52**, 4043–4059.

Numaguti, A., 1993: Dynamics and energy balance of the Hadley circulation and the tropical precipitation zones: Significance of the distribution of evaporation. *J. Atmos. Sci.*, **50**, 1874–1887.

——, M. Takahashi, and A. Sumi, 1995: Development of an atmospheric general circulation model. *Climate System Dynamics and Modeling*, T. Matsuno, Ed., Center for Climate System Research, University of Tokyo, 1–27.

Radke, L. F., J. J. A. Coakley, and M. D. King, 1989: Direct and remote sensing observations of the effects of ships on clouds. *Science*, **246**, 1146–1148.

Rosenfeld, D., 1999: TRMM observed first direct evidence of forest fires inhibiting rainfall. *Geophys. Res. Lett.*, **26**, 3105–3108.

——, 2000: Suppression of rain and snow by urban and industrial air pollution. *Science*, **287**, 1793–1796.

Rotstayn, L. D., 1999: Indirect forcing by anthropogenic aerosols: A global climate model calculation of the effective-radius and cloud-lifetime effects. *J. Geophys. Res.*, **104**, 9369–9380.

Schwartz, S. E., Harshvardhan, and M. Benkovitz, 2002: Influence of anthropogenic aerosol on cloud optical depth and albedo shown by satellite measurements and chemical transport modeling. *Proc. Natl. Acad. Sci. USA*, **99**, 1784–1789.

Squires, P., 1958: The microstructure and colloidal stability of warm

clouds. Part I—The relation between structure and stability. *Tellus*, **10**, 256–261.

Sundqvist, H., 1978: A parameterization scheme for non-convective condensation including prediction of cloud water content. *Quart. J. Roy. Meteor. Soc.*, **104**, 677–690.

Takemura, T., H. Okamoto, Y. Maruyama, A. Numaguti, A. Higurashi, and T. Nakajima, 2000: Global three-dimensional simulation of aerosol optical thickness distribution of various origins. *J. Geophys. Res.*, **105**, 17 853–17 873.

——, T. Nakajima, O. Dubovik, B. N. Holben, and S. Kinne, 2002:

Single scattering albedo and radiative forcing of various aerosol species with a global three dimensional model. *J. Climate*, **15**, 333–352.

Twomey, S., 1974: Pollution and the planetary albedo. *Atmos. Environ.*, **8**, 1251–1256.

——, M. Piepgrass, and T. L. Wolfe, 1984: An assessment of the impact of pollution on global cloud albedo. *Tellus*, **36B**, 356–366.

Wetzel, M. A., and L. L. Stowe, 1999: Satellite-observed patterns in stratus microphysics, aerosol optical thickness, and shortwave radiative forcing. *J. Geophys. Res.*, **104**, 31 287–31 299.